PAPER

2D–2D ZnO/N doped g-C$_3$N$_4$ composite photocatalyst for antibiotics degradation under visible light

Fang Wang,[a] Zhenzhou Zhu [ID] *[b] and Jia Guo*[a]

ZnO and g-C$_3$N$_4$ provide excellent photocatalytic properties for degradation of antibiotics in pharmaceutical wastewater. In this work, 2D–2D ZnO/N doped g-C$_3$N$_4$ (NCN) composite photocatalysts were prepared for degradation of tetracycline (TC), ciprofloxacin (CIP) and ofloxacin (OFLX). The addition of ZnO resulted in higher separation efficiency and lower recombination rate of photogenerated charge under visible light. The composite photocatalyst showed better degradation performance compared to ZnO or NCN alone. The TC degradation reached 81.3% in 15 minutes by applying the prepared 20% ZnO/NCN composite photocatalyst, showing great competitiveness among literature reported g-C$_3$N$_4$ based photocatalysts. After 30 minutes, the degradation rate of TC, CIP and OFLX reached 82.4%, 64.4% and 78.2%, respectively. The TC degradation constant of the composite photocatalyst was 2.7 times and 6.4 times higher than NCN and CN, respectively. Radical trapping experiments indicated that ·O$_2$$^-$ was the dominant active substance. The transference of excited electrons from the conduction band (CB) of NCN to ZnO enhanced the separation of photogenerated electron–hole pairs and simultaneously suppressed their recombination. This study provides a possibility for the design of high-performance photocatalysts for antibiotics degradation in wastewater.

1. Introduction

Pharmaceutically active compounds have become emerging contaminants due to their continuous release and potential threat to the ecological environment and human health. Pharmaceuticals containing antibiotics input to aquatic environments through several pathways, including hospital discharges, domestic wastewater, sewage treatment plants and water treatment plants,[1] at the range of ng L^{-1} to µg L^{-1}.[2,3] Thus, developing innovative technologies for antibiotics treatment with high efficiency is urgent for environmental protection.

Photocatalysis, a kind of advanced oxidation technology, has been widely studied for water purification,[4–6] antibacterial,[7] anti-fog,[8] deodorization,[9] antifouling[10] treatment since it was first reported in 1972.[11] In recent years, a growing body of research was carried out on photocatalytic degradation of antibiotics in pharmaceutical wastewater,[12–16] which was expected to make up for the deficiency of traditional biochemical treatment which is time-consuming and often unreliable.

g-C$_3$N$_4$ is a visible light responsive photocatalyst, which has attracted worldwide attention due to its unique layered structure, innoxious, chemical inertness, low cost, facile fabrication, and appropriate electronic band structure with a band gap of 2.7 eV.[17] These merits make g-C$_3$N$_4$ worthy of being used widely in H$_2$ evolution,[18,19] CO$_2$ reduction,[20] N$_2$ fixation[21] and degradation of pollutants.[12,22] However, pure g-C$_3$N$_4$ tends to suffer unsatisfactory photocatalytic efficiency due to its inherent defects, such as small surface area, fast charge recombination and insufficient utilization of visible light. Till now, variety of modification strategies to address these defects have been made to enhance the efficiency of photocatalytic. Doping, including metal doping, non-metal doping and co-doping, is considered as a practical strategy for tuning the band gap of g-C$_3$N$_4$ for sufficient utilization of visible light.[23] Yan *et al.* fabricated four different metals (Na, K, Ca, Mg) doped g-C$_3$N$_4$, then systematic investigated the different impact on the morphology, structure, and photocatalytic performance. They found the doped metals could introduce structure O into the doped g-C$_3$N$_4$, and simultaneously change its electronic structure which could enhance visible-light harvest and reduce the charges recombination, finally improved the photocatalytic activity.[24] However, the doped heteroatoms as defects may act as a recombination centre for the photo-generated carriers.[25] Therefore, self-doping seems to be a desired method since no heteroatoms will be introduced. Cao *et al.* fabricated a self-carbon doped g-C$_3$N$_4$ composite with dicyanamide as precursor and dimethylformamide as a carbon source. The obtained doped-g-C$_3$N$_4$ displayed

[a]School of Chemical Engineering and Pharmacy, Key Laboratory for Green Chemical Process of Ministry of Education, Key Laboratory of Novel Reactor and Green Chemical Technology of Hubei Province, Wuhan Institute of Technology, Wuhan 430205, PR China. E-mail: guojia@wit.edu.cn

[b]School of Modern Industry for Selenium Science and Engineering, Wuhan Polytechnic University, Wuhan 430023, PR China. E-mail: zhenzhouzhu@126.com

remarkably improved activity of photocatalytic which exhibited 5.2 times higher efficiency compared to pure g-C$_3$N$_4$.[26] Jiang *et al.* prepared N self-doping g-C$_3$N$_4$ nanosheets, which possessed higher photocatalytic performance for degradation of tetracycline (TC) due to the enlarged region of absorption light and improved separation of photogenerated electron–holes.[25] N-doped g-C$_3$N$_4$ was first synthesized by using tiny amounts citric acid as a carbon source to elevate H$_2$ production due to its higher light harvesting, lower charge carrier recombination, and delocalized π-conjugated system extension.[27] Zhu *et al.* subsequently fabricated N-doped g-C$_3$N$_4$ for photodegradation,[28] confirming twice higher photodegradation efficiency than pure g-C$_3$N$_4$.

Apart from doping, construction of heterojunction is another effective way to improve photocatalytic performance due to accelerated separation and transfer efficiency of photogenerated electron–hole pairs.[29] ZnO is a one of the most popular and abundant semiconductor photocatalyst which has a matched band gap with g-C$_3$N$_4$. Many strategies have been made for constructing ZnO/g-C$_3$N$_4$ composite with significant enhancement of photocatalytic activity.[30–32] However, most reported research adopted ZnO with a 3D structure as the chief material, g-C$_3$N$_4$ as the second material accounting for less than 20%.[30,33] Though the tiny g-C$_3$N$_4$ nanosheets could insert into 3D ZnO particles with strong interaction, accelerating the separation of electron–hole pairs, those composites did not show efficient visible light harvest.

Based on the fact that 2D/2D composites possessed lager contact interface and higher efficiency for charges separation and transfer, compared to 2D/3D composites,[34,35] the aim of this study was to construct a new 2D/2D type of ZnO/g-C$_3$N$_4$ composite, with nitrogen doped g-C$_3$N$_4$ as the chief material, for antibiotics treatment under visible light. The chemical composition, morphology and doping structure of the prepared photocatalysts were characterized. The photocatalytic performance was evaluated by the degradation of simulated pharmaceutical wastewater containing tetracycline (TC), ciprofloxacin (CIP) and ofloxacin (OFLX). The photocatalytic mechanism was also proposed after analysis by radicals trapping experiments. This research proposed a new aspect for pharmaceutical wastewater treatment with high efficiency.

2. Experimental

2.1 Materials and reagents

Urea (CO(NH$_2$)$_2$, ≥99.0%), citric acid monohydrate (C$_6$H$_8$O$_7$·H$_2$O, ≥99.5%), zinc acetate (Zn(CH$_3$COO)$_2$·2H$_2$O, ≥99.0%) and hexamethylenetetramine (HMTA, ≥99.0%) were purchased from Sinopharm Chemical Reagent Co., Ltd. Tetracycline hydrochloride (TC, ≥96%) was supplied by Aladdin. Ciprofloxacin (CIP, ≥98%) and ofloxacin (OFLX, ≥98%) were supplied by Maclin. All reagents were used without any further treatment.

2.2 Preparation of photocatalyst

The N-doped g-C$_3$N$_4$ (denoted as NCN) was prepared by a modified method referred to the previous literature.[27,28] In brief, 10 mg citric acid monohydrate was added into 10 g urea and mixed well by gridding during 10 min in an agate mortar, then the mixture was transferred to a covered ceramic crucible in a tube furnace, heated in air to 550 °C with heating rate of 3 °C min^{-1} and maintained for 3 h. Finally, the sample was cooled to room temperature and grounded into fine powders. The pure g-C$_3$N$_4$ (denoted as CN) was prepared in the same condition without addition of citric acid monohydrate.

ZnO was synthesized based on a modified hydrothermal method referred to the previous literature.[36] Typically, 1.32 g zinc acetate dihydrate and 0.86 g hexamethylenetetramine (HMTA) were dissolved in 50 mL and 10 mL distilled water, respectively. Then the HMTA solution was dropped into zinc acetate solution, the mixture was stirred for 1 h in room temperature, and then transferred into a 100 mL Teflon-lined stainless-steel autoclave, kept at 150 °C for 8 h. The obtained precipitates were washed with distilled water followed by centrifugation for several times and dried at 60 °C overnight. Finally, the ZnO powders were calcined at 400 °C for 2 h.

ZnO/NCN composites were prepared by a self-assembled method through electrostatic attraction, which was confirmed to be practicable.[37] Take 20% ZnO/NCN composites preparation for example, 0.1 g NCN powder was added into 50 mL DI water and sonicated for 1 h, then 0.02 g ZnO powder was well dispersed in 10 mL DI water and then dropped into NCN solution, after stirred over a night, the mixed solution was filtrated and dried at 60 °C for 8 h, then grinded into fine powders. For comparison, 10% ZnO/NCN, 30% ZnO/NCN and 20% ZnO/CN composites catalysts were prepared.

2.3 Characterization

X-ray diffraction (XRD) patterns were obtained by Bruker D8 Advance with Cu Kα radiation at a scanning speed of 5°/min. Fourier transformed infrared (FTIR) spectra were conducted by a FTIR spectrometer (Nicolet 6700, USA). The morphologies of the prepared samples were observed by SEM (Zeiss Gemini 300) and TEM (JEM-2100F) images. The BET specific surface area and nitrogen adsorption–desorption isotherms were obtained using an Autosorb iQ instrument (Quantachrome Instruments). X-ray photoelectron spectroscopy (XPS) was carried out on a Thermo Scientific K-Alpha spectrometer. The UV-vis diffuse reflection spectra (DRS) were recorded by a UV-Vis spectrophotometer (PerkinElmer Lambda 750S, USA). The steady-state photoluminescence (PL) of samples were measured by FLS1000 (Edinburgh Instruments) with a Xe-lamp under the excitation of 325 nm.

2.4 Photocatalytic evaluation

The photocatalytic performance of catalysts was evaluated by degradation of tetracycline (TC) (20 mg L^{-1}) solution, ciprofloxacin (CIP) (10 mg L^{-1}) solution and ofloxacin (OFLX) (10 mg L^{-1}) solution. 20 mg catalyst was dispersed in 200 mL simulated wastewater, then stirred in dark for 30 min for adsorption–desorption equilibrium. Then photocatalytic reaction was performed under a 300 W xenon lamp (PLS-SXE300) with a 420 nm cut-off filter as visible light source. In the

reaction process, about 2 mL solution was taken out at regular time, and filtrated through a 0.22 μm filter to remove the catalyst. The concentration of the wastewater was measured by a UV-Vis spectrophotometer at 357 nm for TC, 274 nm for CIP, and 286 nm for OFLX. To evaluate the stability of the composite photocatalyst, the recyclability evaluation test had been carried out. The test was assessed under the same condition of the TC photodegradation by using the same photocatalyst 3 times. Typically, after each degradation process, the photocatalyst was collected by suction filtration with thoroughly washed by DI water, and then dried at 60 °C.

2.5 Radicals trapping experiments

In order to figure out the dominating active species during the photocatalytic process, benzoquinone (BQ), isopropanol (IPA)

and ethylenediamine tetra acetic acid disodium salt (EDTA-2Na) were added into the TC solution to capture superoxide radicals ($\cdot O_2^-$), hydroxyl radicals ($\cdot OH$), and the holes (h^+) respectively. Furthermore, Electron Spin Resonance (ESR) was carried out to detect the existence of $\cdot O_2^-$ radicals in methanol solution with DMPO as scavenger by Bruker EMXPLUS.

3. Results and discussion

3.1 Characterization of composite photocatalyst

XRD was carried out to characterize the composition and crystalline structure of the as-prepared photocatalysts. As shown in Fig. 1, NCN and CN both have two diffraction peaks at 13° (001) and 27.6°(002), which were corresponding to heptazine units in the plane with a d-spacing of 0.67 nm and interlayer stacking of conjugated aromatic rings with a d-spacing of 0.33 nm, respectively.[18,38] The two similar peaks evidenced the same structure of NCN and CN. The wider (002) peek of NCN illustrated that the interlayer structure was destroyed slightly after nitrogen doping. For the pure ZnO, the peaks located at 31.8° (100), 34.5° (002), 36.3° (101), 47.65° (102), 56.7° (110), 63.0° (103) and 68.1° (112) were highly consistent with the standard data of ZnO hexagonal wurtzite phase (JCPDS no. 75-0576). For the composite photocatalysts, all peaks in pure ZnO and NCN can be found, and the intensity of the peaks belong to NCN became weaker as the proportion of ZnO increased. The XRD results demonstrated that the composite photocatalysts ZnO/NCN were successfully fabricated.

The functional groups of the catalysts can be confirmed by FTIR spectroscopy. As shown in Fig. 2(a), the characteristic spectrums of these three catalysts (CN, NCN, 20% ZnO/NCN) were similar, also illustrated that the NCN catalyst have the same chemical structure with CN. The peak at 812 cm^{-1} was derived from the breathing mode of triazine unit,[38] and the small peak at 882 cm^{-1} attributed to deformation mode of N–
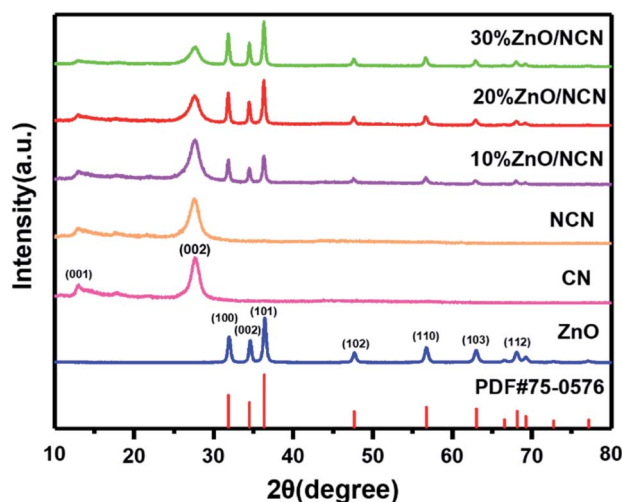

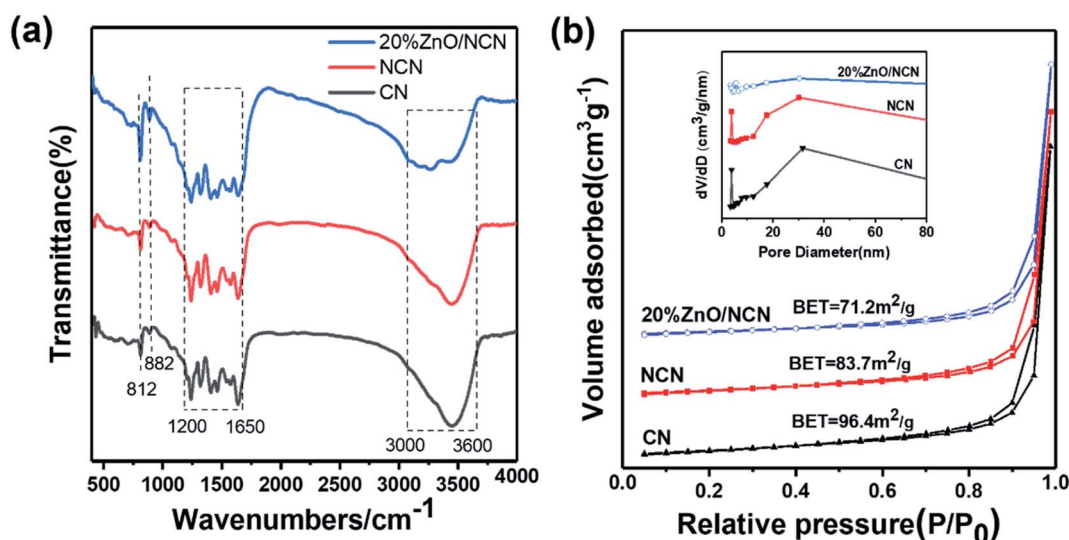**Fig. 1** XRD patterns of the as-prepared photocatalysts.

Fig. 2 (a) FTIR spectra and (b) N$_2$ adsorption–desorption isotherms of CN, NCN, and 20% ZnO/NCN. Corresponding pore-size distribution of CN, NCN, and 20% ZnO/NCN were inserted in Fig. 2(b).

H.[39] The peaks in the range of 1238 to 1637 cm^{-1} were originated from different vibration modes of C–N and C=N bond in triazine unit.[40] The broad absorption band from 3000 to 3600 cm^{-1} can be ascribed to the stretching vibration of N–H and O–H bond contributed to uncondensed amine group and the absorption of water molecules on sample surfaces, respectively.

Fig. 2(b) displayed the N_2 adsorption–desorption isotherms of CN, NCN, and 20% ZnO/NCN. As shown in the figure, all samples have the similar type IV isotherm, which demonstrated the existence of mesopores. Furthermore, all the hysteresis loops belong to H3 type, the adsorption capacity increased rapidly at high relative pressure, caused by the slit-like pores formed by the aggregates of flaky particles, which corresponded to the result of SEM. The pore-size distribution inserted in Fig. 2(b) suggested that all samples both existed mesopores (~5 nm) and macropores (20–80 nm) with the average pore size of ~30 nm. Additionally, the specific surface area of 20% ZnO/NCN composite catalyst was declined by 15% compared to NCN (from 83.7 $m^2 g^{-1}$ to 71.2 $m^2 g^{-1}$), due to the small specific surface area of ZnO.

The morphologies and structures of CN, NCN, ZnO and 20% ZnO/NCN were characterized by SEM and TEM (Fig. 3). The Fig. 3(a) and (b) indicated that both CN and NCN exhibited
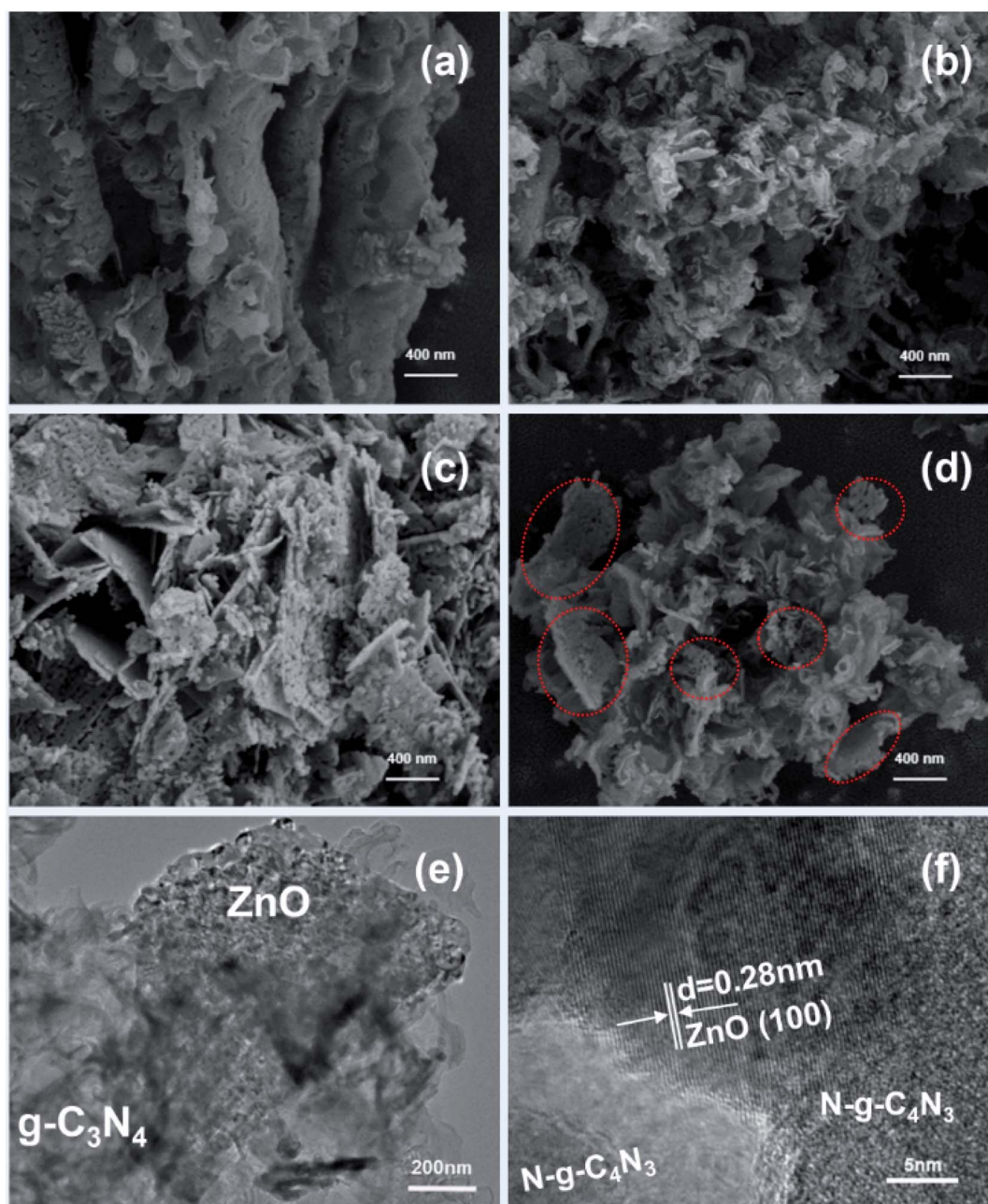

Fig. 3 SEM images of CN (a), NCN (b), ZnO (c) and 20% ZnO/NCN (d), and TEM of 20% ZnO/NCN (e and f).

a nanoscale lamellar structure with some little pores. Nevertheless, the sheet size of the sample NCN is much smaller, thinner and frizzier at the edge. Fig. 3(c) presents the morphology of ZnO. Obviously, the sample displayed a porous two-dimensional (2D) nanosheet morphology with no aggregation, and the porous structure may be caused by decomposing of the residual zinc acetate in calcination process. This 2D structure makes it more compatible with other 2D materials. As shown in Fig. 3(d), the 2D ZnO nanosheets (red circle marked) were inserted into NCN nanosheet. The TEM results could further demonstrate the combination of the two materials, as shown in Fig. 3(e). Moreover, the lattice fringes of ZnO can be clearly seen in HR-TEM image (Fig. 3(f)), the interplanar spacing of 0.28 nm stemmed from ZnO (100),[41] which were consistent with the test of XRD.

XPS was applied to investigate the chemical state of photocatalysts surfaces. Fig. 4(a)–(d) shows the survey spectra and high-resolution XPS spectra of C 1s, N 1s and Zn 2p of CN, NCN, ZnO and 20% ZnO/NCN photocatalysts, respectively. From the

full survey spectra (Fig. 4(a)), the characteristic peaks of Zn 2p, O 1s, N 1s and C 1s can be found for the 20% ZnO/NCN composite. Fig. 4(b) shows that CN, NCN and 20% ZnO/NCN samples have similar C 1s spectra with three peaks at about 284.8 eV, 286.5 eV and 288.2 eV. The peak at 284.8 eV corresponded to C–C bonds of graphitic carbon or adventitious carbon.[28] The minor peak at 286.5 eV was assigned to $C–NH_2$ bonds at edges of heptazine units which became stronger after N doping.[41] The main peak at about 288.2 eV can be attributed to N=C–N bonds in heptazine units. As shown in Fig. 4(c), N 1s spectra can be divided into four peaks at about 398.6 eV, 399.8 eV, 401.1 eV and 404.3 eV, which were attributed to sp^2-hybridized nitrogen (C–N=C), tertiary nitrogen $N-(C)_3$ groups in heptazine units, uncondensed amino groups (C–N–H or $C–NH_2$),[28] and π excitation, respectively. In Zn 2p spectra (Fig. 4(d)), the peaks at 1045.5 eV and 1022.5 eV were ascribed to Zn $2p_{1/2}$ and Zn $2p_{3/2}$.[42] Compared to pure ZnO, the binding energy of Zn 2p exhibited a negative shift in 20% ZnO/NCN composite photocatalyst, which may be due to
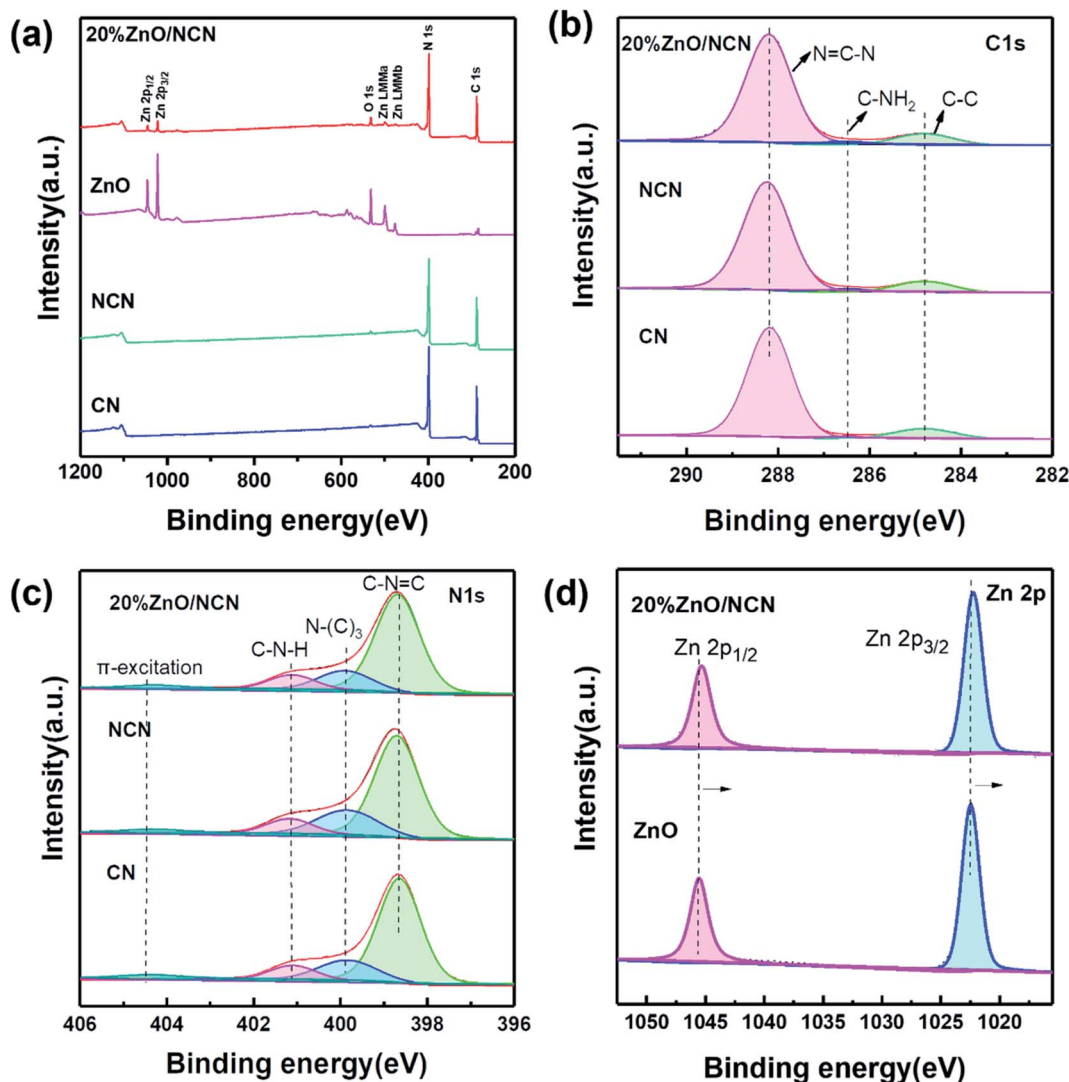
Fig. 4 XPS spectra of (a) survey spectra, (b) C 1s, (c) N 1s of CN, NCN, 20% ZnO/NCN, and (d) Zn 2p of ZnO and 20% ZnO/NCN.
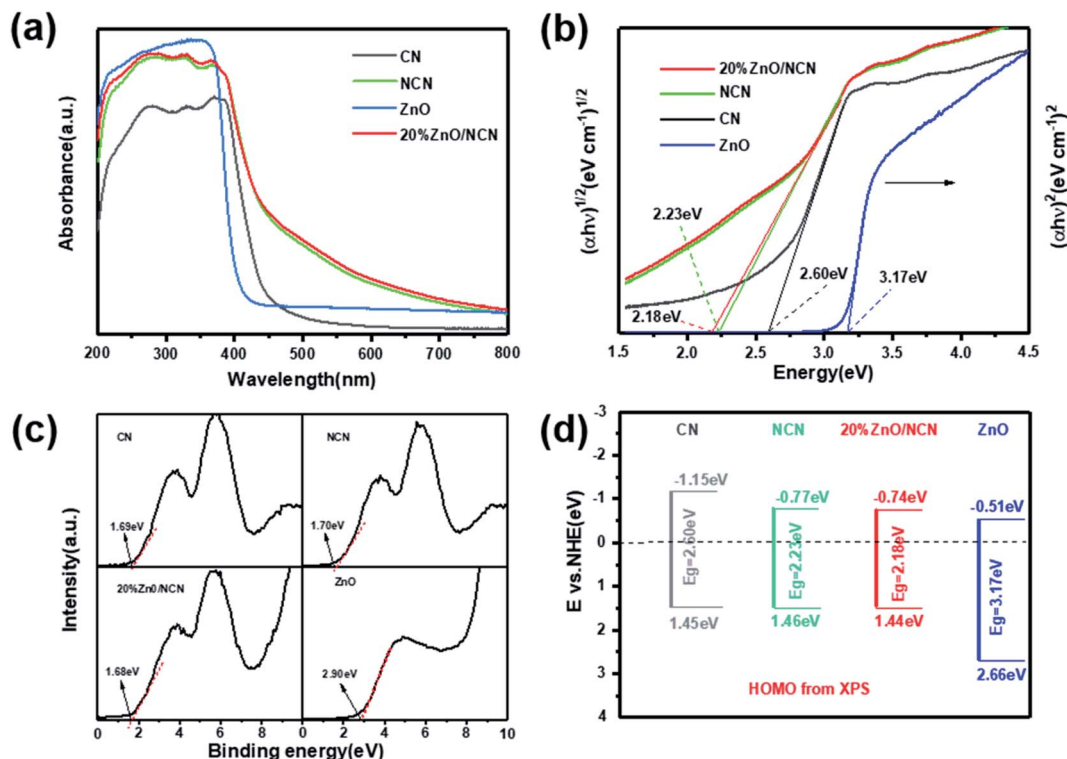
Fig. 5 (a) The UV-vis diffuse reflectance spectra (DRS), (b) the Tauc-plots, (c) VB XPS spectra, and (d) the band structure of CN, NCN, ZnO and 20% ZnO/NCN.

the transfer of electrons from NCN to ZnO, revealing that there was a strong interaction between ZnO and NCN.

3.2 Photoelectric properties

The UV-vis DRS of the as-prepared photocatalysts were shown in Fig. 5(a). Compared to CN, the absorption edge of NCN exhibited a distinct red shift, meanwhile, the absorption intensity of NCN increased obviously, even in the visible light region (λ > 420 nm), which would boost visible light harvesting greatly. For pure ZnO, the absorption intensity was strong but only in UV region (λ < 400 nm).[32] However, after composited with NCN, 20% ZnO/NCN possessed a similar light absorption character with NCN, meaning that the addition of ZnO didn't

reduce the efficiency of light absorption of NCN. These results indicated the formation of heterojunction between NCN and ZnO, rather than a simple mechanical mixture.

The bandgap energy values (E_g) can be extracted from the DRS spectra through Tauc-plots by the formula: $\alpha h\nu = A(h\nu - E_g)^n$, where α, h and ν represent absorption coefficient, Planck constant and light frequency, and n is 2 for direct semi-conductor, while 0.5 for indirect semiconductor.[17] CN is an indirect semiconductor,[22,29] and ZnO is a direct semi-conductor.[43,44] As shown in Fig. 5(b), the bandgap energy values were 2.6 eV, 2.23 eV, 2.18 eV and 3.17 eV for CN, NCN, 20% ZnO/NCN and ZnO, respectively. Compared to CN, NCN had a narrower bandgap. The bandgap of the composited photocatalyst
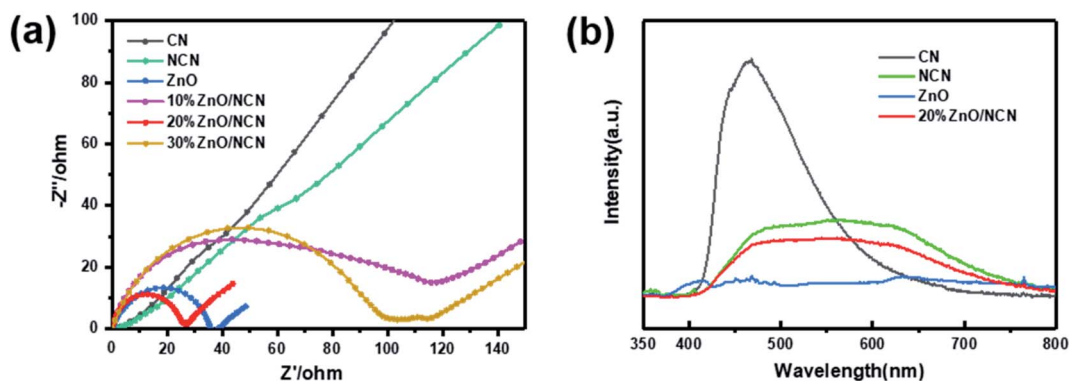

Fig. 6 (a) EIS Nyquist plots and (b) steady-state photoluminescence spectra (PL) (under 325 nm excitation) of the as-prepared photocatalysts.
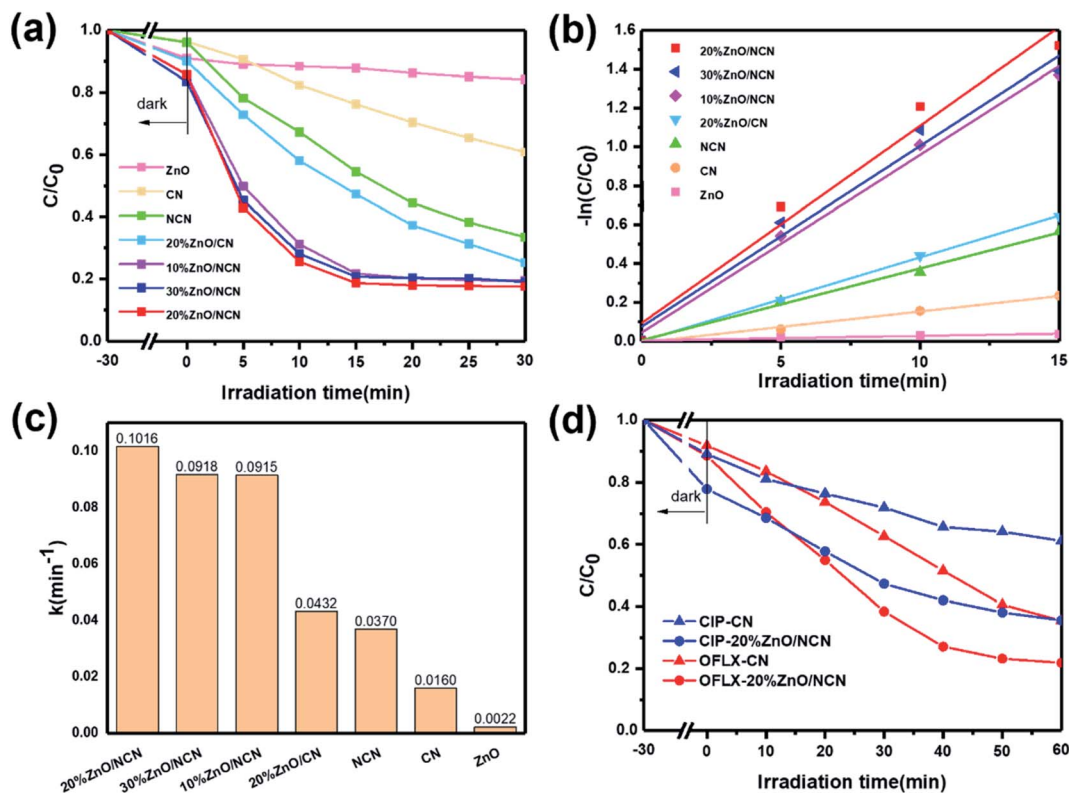
Fig. 7 Photocatalytic activities of as-prepared photocatalysts: (a) degradation of 20 mg L⁻¹ TC under visible light irradiation (λ > 420 nm); (b) first-order kinetic plots of TC; (c) degradation rates of TC; (d) degradation efficiency of CIP and OFLX by NCN and 20% ZnO/NCN. [TC] = 20 mg L⁻¹, [CIP] = 10 mg L⁻¹, [OFLX] = 10 mg L⁻¹, [catalyst] = 0.1 g L⁻¹.

Table 1 A summary of photocatalytic degradation of TC over reported g-C₃N₄-based photocatalysts

Photocatalyst	$C_{catalyst}$ (g L⁻¹)	C_{TC} (mg L⁻¹)	Light source	Degradation rate (%)	Reference
Ag₃PO₄/g-C₃N₄/ZnO	0.4	30	45 W, visible lamp	85.91%, 2 h	20
Ag/g-C₃N₄	1.67	20	300 W (λ > 420 nm) Xe lamp	83%, 120 min	45
g-C₃N₄/PW₁₂/TiO₂	1	40	300 W (λ > 420 nm) Xe lamp	85.01%, 50 min	46
C₃N₄/WO₃	0.4	10	500 W (λ > 320 nm) Xe lamp	79.8%, 180 min	47
CuInS₂/g-C₃N₄	0.5	20	300 W (λ > 420 nm) Xe lamp	83.7%, 60 min	35
ZnSnO₃/g-C₃N₄	0.5	10	300 W (λ > 420 nm) Xe lamp	85%, 120 min	48
ZnO/NCN	0.1	20	300 W (λ > 420 nm) Xe lamp	81.3%, 15 min	This work

20% ZnO/NCN was observed similar with NCN, which makes them more easily to be excited by visible light. In order to calculate the relative positions of valence band, VB XPS had been carried out. Fig. 5(c) showed the values of valence band maximum (VBM) of the as-prepared photocatalysts, which were the contact potential difference between the samples and the analyzer, and that can be converted to E_{VB} vs. NHE through the formula $E_{NHE}/V = \phi + VBM - 0.44$ (E_{NHE}: potential of normal hydrogen electrode; ϕ of 4.2 eV: the electro work function of the analyzer).[18,39,40] Otherwise, using the formula $E_{CB} = E_{VB} - E_g$,[31] and combined with the values of E_g obtained from DRS spectra, the values of E_{CB} can be gained. The band structure of the as-prepared photocatalysts was shown in Fig. 5(d). CN, NCN and 20% ZnO/NCN nearly possessed the same valence band value, indicated that either nitrogen doping nor composite with ZnO

did not change the valence band, but the E_{CB} decreased from −1.15 eV to −0.74 eV, leading to a narrower band gap.

The electrochemical impedance spectra (EIS) and steady-stable photoluminescence spectra (PL) showed separation efficiency and transfer ability of the photogenerated charge. As indicated in Fig. 6(a), 20% ZnO/NCN composite photocatalyst had the smallest arc radical, which indicated a smallest charge transfer resistance. It also means the highest photogenerated charge separation efficiency and transfer ability. Fig. 6(b) showed the PL spectra of CN, NCN, ZnO and 20% ZnO/NCN excited at 325 nm. The pure CN possessed a strong emission peak at about 470 nm, which occurs during carrier recombination. While, after nitrogen doping, the emission peak had a red-shift, and the intensity was obviously decreased, which means a less recombination of the photogenerated charge. For
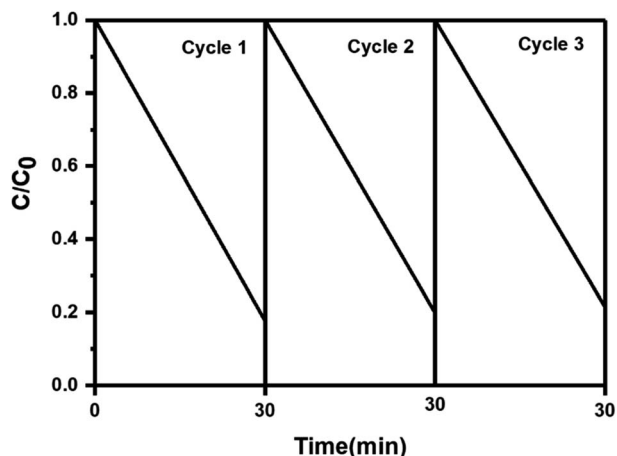
Fig. 8 The recyclability evaluation of 20% ZnO/NCN for the photo-degradation of TC (20 mg L^{-1}) under visible light irradiation ($\lambda > 420$ nm).

results. Moreover, when NCN was composited with ZnO, the degradation speed of TC increased rapidly, especially for 20% ZnO/NCN. This may be explained by the explained by the transference of excited electrons from NCN to ZnO, which enhanced the separation of electrons and holes. For 20% ZnO/NCN, the degradation rate could reach up to about 81.3% in 15 min under visible light irradiation. However, it increased a little when reaction time was prolonged to 30 min, which may be due to insufficient oxidation capacity and low concentration of the solution. Notably, with the increase of the proportion of ZnO, the activity of composite photocatalyst decreased slightly, because excessive ZnO particles may act as recombination centres of the photo-induced carriers.[41,49]

The TC degradation under visible light by the as-prepared catalysts in the first 15 min conformed to pseudo-first-order kinetics model, depicting in Fig. 7(b) and (c), and 20% ZnO/NCN composite catalyst showed the highest degradation constant (0.1016 min^{-1}), which was 2.7 times and 6.4 times higher compared to NCN and CN, respectively. The photocatalyst with high degradation constant is preponderant in practical application, so it can increase efficiency and save cost. Additionally, a comparison of TC degradation between different g-C$_3$N$_4$-based photocatalysts have been summarized in Table 1. As can be seen, there are obvious advantages for 20% ZnO/NCN constructed in this work, with less photocatalyst dosage but greater degradation rate.

In order to further illustrate the application of composite photocatalysts for pharmaceutical wastewater treatment, degradation of ciprofloxacin (CIP) and ofloxacin (OFLX) were also carried out. As shown in Fig. 7(d), degradation of CIP and OFLX were observed under both NCN and 20% ZnO/NCN treatment, while CIP was relatively more persistent compared to OFLX. By 20% ZnO/NCN composite catalyst, the degradation rate of OFLX and CIP could achieve 78.2% and 64.4%, respectively. Which was 1.2 times and 1.7 times, respectively, compared to the NCN catalyst.

The stability of photocatalysts is another vital index to evaluate the performance of photocatalytic, which is important in practical application. Fig. 8 showed the results of recyclability
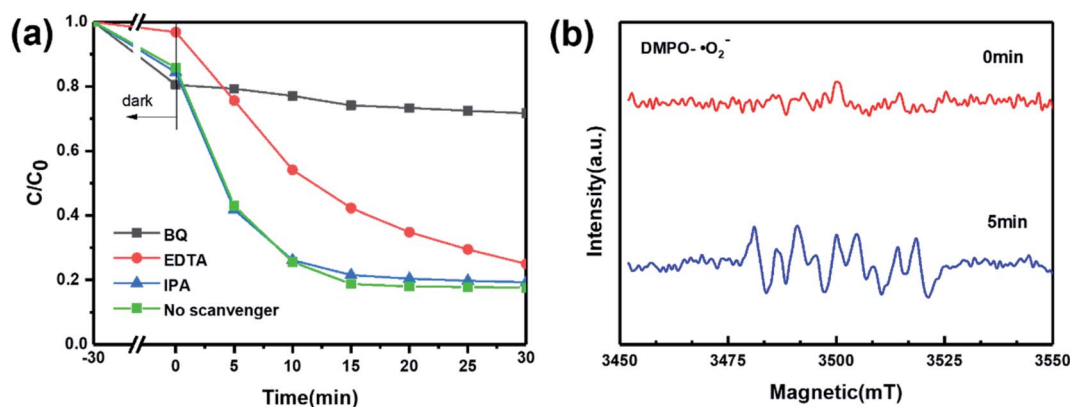
20% ZnO/NCN, the emission peak was further decreased, this result was consistent with the EIS analysis. Both EIS and PL spectra demonstrated that the composite photocatalyst 20% ZnO/NCN possessed a high photogenerated charge separation efficiency, faster transfer ability and lower recombination rate simultaneously.

3.3 Photocatalytic performance

To evaluate the activity of the as-prepared photocatalysts, TC (20 mg L^{-1}), CIP (10 mg L^{-1}) and OFLX (10 mg L^{-1}) were selected as simulated pharmaceutical wastewater for degradation experiments under visible light ($\lambda > 420$ nm). Pure ZnO and CN showed low degradation efficiency for TC (Fig. 7(a)). However, after nitrogen doping, the degradation efficiency for NCN was enhanced significantly (from 39.1% to 66.5%), which was about 1.7 times compare to CN, demonstrating that nitrogen doping could improve photocatalytic activity, which due to the narrower band gap as well as lower recombination rate of electrons and holes according to UV-Vis and PL spectra

Fig. 9 (a) Photodegradation of TC (20 mg L^{-1}) by 20% ZnO/NCN in the presence of scavengers, and (b) ESR spectroscopy of 20% ZnO/NCN for $\cdot$O$_2^-$ radicals detected in methanol solution with DMPO as scavenger under visible light irradiation ($\lambda > 420$ nm).
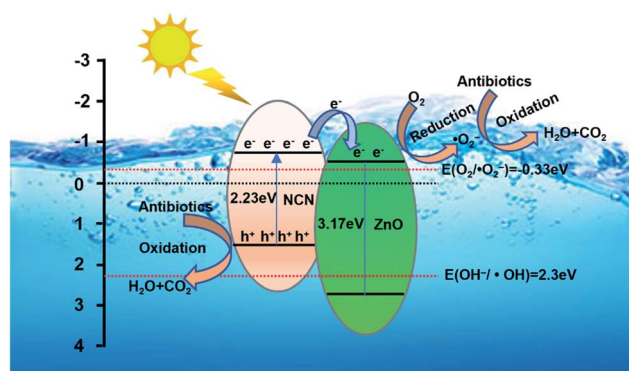
Fig. 10 The possible mechanism for photodegradation of antibiotics by 20% ZnO/NCN under visible light irradiation.

evaluation test, after 3 cycling photodegradation of TC, the degradation efficiency declined a little (from 82.4% to 78.6%), suggesting that this composite photocatalyst will be quite stable in practical application.

3.4 Photocatalytic mechanism

In order to explore the photodegradation mechanism of antibiotics, the dominant active species during the photodegradation process should be identified. Benzoquinone (BQ) was used for capturing superoxide radicals ($\cdot O_2^-$), isopropanol (IPA) for hydroxyl radicals ($\cdot OH$), and ethylenediamine tetra acetic acid disodium salt (EDTA-2Na) for the holes (h^+). As presented in Fig. 9(a), the degradation rate was declined from 82.4% to 28.3% in the presence of BQ, demonstrated that $\cdot O_2^-$ was the dominant active substance. Besides, degradation efficiency decreased with the EDTA-2Na addition, indicated that h^+ is a secondary active substance. However, when IPA was added, there was no obvious changes on the degradation efficiency, illustrating that $\cdot OH$ radicals were negligible. Furthermore, ESR was carried out to detect the existence of $\cdot O_2^-$ radicals in methanol solution with DMPO as a scavenger. As shown in Fig. 9(b), under the irradiation of visible light ($\lambda > 420$ nm) for 5 min, the DMPO-$\cdot O_2^-$ signal peak was significant enhanced, which further proved the generation of $\cdot O_2^-$ radicals in the degradation process by 20% ZnO/NCN.

As can be seen from the XPS results, the binding energy of Zn 2p was increased, indicated that ZnO gained electrons from NCN, while considering that under visible light ($\lambda > 420$ nm) irradiation, only NCN can be excited, so combined with these results, a possible mechanism for photodegradation of antibiotics by 20% ZnO/NCN under visible light irradiation was proposed in Fig. 10. The photogenerated electrons (e^-) on the CB of NCN transferred to the CB of ZnO, while the holes (h^+) still remain on the VB of NCN. The accumulated electrons (e^-) on the CB of ZnO which can reduce the adsorbed O_2 to $\cdot O_2^-$ radicals, and the $\cdot O_2^-$ radicals reacted with antibiotics then degraded them to CO_2 and H_2O. Meanwhile, the holes (h^+) on the VB of NCN which can directly oxidize antibiotics to CO_2 and H_2O. The electrons transferred from NCN to ZnO in 20% ZnO/NCN composite can efficiently enhance the separation of

photogenerated electron–hole pairs and simultaneously suppressed their recombination, hence the photodegradation efficiency of antibiotics was enhance significantly.

4. Conclusions

ZnO/NCN composite photocatalyst with N doped g-C$_3$N$_4$ as dominant material was prepared for photodegradation of antibiotics under visible light irradiation. Physicochemical characterizations evidenced the 2D–2D structure and the formation of the composite photocatalyst. Although the addition of ZnO did not change the band structure of NCN, it led to higher separation efficiency and lower recombination rate of photogenerated charge. The composite photocatalyst showed competitive degradation ability for TC, CIP and OLFX, compared to previous literature works. Especially, the 20% ZnO/NCN composite catalyst showed the highest TC degradation constant (0.1016 min^{-1}), which was 2.7 times higher than NCN, and 6.4 times higher than CN. Photocatalytic mechanism analysis indicated that $\cdot O_2^-$ was the dominant active substance, and the transference of excited electrons from the CB of NCN to ZnO enhanced the separation of photogenerated electron–hole pairs and simultaneously suppressed their recombination.

Author contributions

Dr Fang Wang: carrying out experiments, manuscript writing. Prof. Zhenzhou Zhu: resources, manuscript revising. Prof. Jia Guo: experiments design, manuscript revising.

Conflicts of interest

There are no conflicts to declare.

Acknowledgements

References

1 Y. Yang, Y. S. Ok, K. H. Kim, E. E. Kwon and Y. F. Tsang, *Sci. Total Environ.*, 2017, **596–597**, 303–320.

2 J. L. Liu and M. H. Wong, *Environ. Int.*, 2013, **59**, 208–224.

3 S. Zhou, C. Di Paolo, X. Wu, Y. Shao, T. B. Seiler and H. Hollert, *Environ. Int.*, 2019, **128**, 1–10.

4 K. Li, J. Chen, Y. Ao and P. Wang, *Sep. Purif. Technol.*, 2021, **259**, 118177.

5 H. R. Zhang, A. U. Mane, X. B. Yang, Z. J. Xia, E. F. Barry, J. Q. Luo, Y. H. Wan, J. W. Elam and S. B. Darling, *Adv. Funct. Mater.*, 2020, **30**, 9.

6 G. D. Fan, Z. Chen, Z. S. Yan, B. H. Du, H. L. Pang, D. S. Tang, J. Luo and J. Y. Lin, *J. Hazard. Mater.*, 2021, **409**, 15.

7 Z. Y. Teng, N. L. Yang, H. Y. Lv, S. C. Wang, M. Z. Hu, C. Y. Wang, D. Wang and G. X. Wang, *Chem*, 2019, **5**, 664–680.

8 Y. Zhang, S. Zhang and S. Wu, *Chem. Eng. J.*, 2019, **371**, 609–617.

9 S.-H. Jo, K.-H. Kim, Y.-H. Kim, M.-H. Lee, B.-W. Kim and J.-H. Ahn, *Chem. Eng. J.*, 2015, **277**, 260–268.

10 S. J. You, G. U. Semblante, S. C. Lu, R. A. Damodar and T. C. Wei, *J. Hazard. Mater.*, 2012, **237–238**, 10–19.

11 A. Fujishima and K. Honda, *Nature*, 1972, **238**, 37–38.

12 S. Adhikari, H. H. Lee and D.-H. Kim, *Chem. Eng. J.*, 2020, **391**, 123504.

13 W. Zhu, F. Sun, R. Goei and Y. Zhou, *Catal. Sci. Technol.*, 2017, **7**, 2591–2600.

14 H. Wang, C. Y. Zhang, T. L. Chang, J. Z. Su and L. J. Ci, *J. Mater. Sci.: Mater. Electron.*, 2021, **32**, 2822–2831.

15 W. Shi, S. Yang, H. Sun, J. Wang, X. Lin, F. Guo and J. Shi, *J. Mater. Sci.*, 2021, **56**, 1–15.

16 J. Piriyanon, T. Chankhanittha, S. Youngme, K. Hemavibool and S. Nanan, *J. Mater. Sci.: Mater. Electron.*, 2021, **32**, 1–22.

17 F. Dong, L. Wu, Y. Sun, M. Fu, Z. Wu and S. C. Lee, *J. Mater. Chem.*, 2011, **21**, 15171.

18 Y.-S. Jun, E. Z. Lee, X. Wang, W. H. Hong, G. D. Stucky and A. Thomas, *Adv. Funct. Mater.*, 2013, **23**, 3661–3667.

19 X. Li, W. Bi, L. Zhang, S. Tao, W. Chu, Q. Zhang, Y. Luo, C. Wu and Y. Xie, *Adv. Mater.*, 2016, **28**, 2427–2431.

20 P. Zhu, M. Hu, M. Duan, L. Xie and M. Zhao, *J. Alloys Compd.*, 2020, **840**, 155714.

21 P. Qiu, Z. Liang, X. Liu, X. Qian, H. Cui and J. Tian, *J. Colloid Interface Sci.*, 2020, **571**, 318–325.

22 H. Huang, Y. Li, H. Wang and W. Jiang, *Appl. Surf. Sci.*, 2021, **538**, 148132.

23 L. Jiang, X. Yuan, Y. Pan, J. Liang, G. Zeng, Z. Wu and H. Wang, *Appl. Catal., B*, 2017, **217**, 388–406.

24 W. Yan, L. Yan and C. Jing, *Appl. Catal., B*, 2019, **244**, 475–485.

25 L. Jiang, X. Yuan, G. Zeng, J. Liang, Z. Wu, H. Yu, D. Mo, H. Wang, Z. Xiao and C. Zhou, *J. Colloid Interface Sci.*, 2019, **536**, 17–29.

26 J. S. Cao, H. Q. Fan, C. Wang, J. W. Ma, G. Z. Dong and M. C. Zhang, *Ceram. Int.*, 2020, **46**, 7888–7895.

27 Y.-j. Zhou, L.-x. Zhang, W.-m. Huang, Q.-l. Kong, X.-q. Fan, M. Wang and J.-l. Shi, *Carbon*, 2016, **99**, 111–117.

28 D. Zhu and Q. Zhou, *Appl. Catal., B*, 2021, **281**, 119474.

29 J. Fu, J. Yu, C. Jiang and B. Cheng, *Adv. Energy Mater.*, 2018, **8**, 1701503.

30 J. Wang, Y. Xia, H. Zhao, G. Wang, L. Xiang, J. Xu and S. Komarneni, *Appl. Catal., B*, 2017, **206**, 406–416.

31 X. Tan, X. Wang, H. Hang, D. Zhang, N. Zhang, Z. Xiao and H. Tao, *Opt. Mater.*, 2019, **96**, 109266.

32 S. Liu, F. Li, Y. Li, Y. Hao, X. Wang, B. Li and R. Liu, *Appl. Catal., B*, 2017, **212**, 115–128.

33 N. Kumaresan, M. M. A. Sinthiya, M. Sarathbavan, K. Ramamurthi, K. Sethuraman and R. R. Babu, *Sep. Purif. Technol.*, 2020, **244**, 116356.

34 J. He, J. Yang, F. Jiang, P. Liu and M. Zhu, *Chemosphere*, 2020, **258**, 127339.

35 F. Guo, W. Shi, M. Li, Y. Shi and H. Wen, *Sep. Purif. Technol.*, 2019, **210**, 608–615.

36 F. Liu, X. Wang, X. Chen, X. Song, J. Tian and H. Cui, *ACS Appl. Mater. Interfaces*, 2019, **11**, 24757–24763.

37 N. Nie, L. Zhang, J. Fu, B. Cheng and J. Yu, *Appl. Surf. Sci.*, 2018, **441**, 12–22.

38 P. Niu, L. Zhang, G. Liu and H.-M. Cheng, *Adv. Funct. Mater.*, 2012, **22**, 4763–4770.

39 J. Wen, J. Xie, X. Chen and X. Li, *Appl. Surf. Sci.*, 2017, **391**, 72–123.

40 P. Xia, B. Zhu, J. Yu, S. Cao and M. Jaroniec, *J. Mater. Chem. A*, 2017, **5**, 3230–3238.

41 L. Huang, D. Bao, J. Li, X. Jiang and X. Sun, *Appl. Surf. Sci.*, 2021, **555**, 149696.

42 D. Shen, X. Li, C. Ma, Y. Zhou, L. Sun, S. Yin, P. Huo and H. Wang, *New J. Chem.*, 2020, **44**, 16390–16399.

43 H. L. Guo, Q. Zhu, X. L. Wu, Y. F. Jiang, X. Xie and A. W. Xu, *Nanoscale*, 2015, **7**, 7216–7223.

44 S. Liu, L. Zhu, W. Cao, P. Li, Z. Zhan, Z. Chen, X. Yuan and J. Wang, *J. Alloys Compd.*, 2021, **858**, 157654.

45 W. Xu, S. Lai, S. C. Pillai, W. Chu, Y. Hu, X. Jiang, M. Fu, X. Wu, F. Li and H. Wang, *J. Colloid Interface Sci.*, 2020, **574**, 110–121.

46 H. Shi, T. Zhao, J. Wang, Y. Wang, Z. Chen, B. Liu, H. Ji, W. Wang, G. Zhang and Y. Li, *J. Alloys Compd.*, 2021, **860**, 157924.

47 H. Jing, R. Ou, H. Yu, Y. Zhao, Y. Lu, M. Huo, H. Huo and X. Wang, *Sep. Purif. Technol.*, 2021, **255**, 117646.

48 X. Huang, F. Guo, M. Li, H. Ren, Y. Shi and L. Chen, *Sep. Purif. Technol.*, 2020, **230**, 115854.

49 M. A. Qamar, S. Shahid and M. Javed, *Ceram. Int.*, 2020, **46**, 22171–22180.